Hindawi
Shock and Vibration
Volume 2021, Article ID 6547028, 18 pages
https://doi.org/10.1155/2021/6547028

Research Article

Study on Mesoscopic Damage Evolution Characteristics of Single Joint Sandstone Based on Micro-CT Image and Fractal Theory

Hao Liu,[1,2,3] Lulin Zheng,[1] Yujun Zuo,[1,2] Zhonghu Wu,[4] Wenjibin Sun,[1] Lujing Zheng,[1] Chao Pan,[1] Jianyun Lin,[1,2] Zehua Zhu,[1] and Zhibin Hao[1]

[1]*Mining College, Guizhou University, Guiyang 550025, Guizhou, China*
[2]*School of Resource and Environmental Engineering, Guizhou University, Guiyang 550025, Guizhou, China*
[3]*Department of Civil and Environmental Engineering, Technical University of Catalonia (UPC), 08034, Spain*
[4]*College of Civil Engineering, Guizhou University, Guiyang 550025, Guizhou, China*

Correspondence should be addressed to Lulin Zheng; llzheng@gzu.edu.cn

Received 3 August 2021; Revised 10 September 2021; Accepted 15 September 2021; Published 5 October 2021

Academic Editor: Lishuai Jiang

The different directions of joints in rock will lead to great differences in damage evolution characteristics. This study utilizes DIP (digital image processing) technology for characterizing the mesostructure of sandstone and combines DIP technology with RFPA2D. The mesoscale fracture mechanics behavior of 7 groups of jointed sandstones with various dip angles was numerically studied, and its reliability was verified through theoretical analysis. According to digital image storage principle and box dimension theory, the box dimension algorithm of rock mesoscale fracture is written in MATLAB, the calculation method of fractal dimension of mesoscale fracture was proposed, and the corresponding relationship between mesoscale fractal dimension and fracture damage degree was established. Studies have shown that compressive strength as well as elastic modulus of sandstone leads to a U-shaped change when joint dip increases. There are a total of six final failure modes of joint samples with different inclination angles. Failure mode and damage degree can be quantified by D (fractal dimension) and ω (mesoscale fracture damage degree), respectively. The larger the ω, the more serious the damage, and the greater the D, the more complex the failure mode. Accumulative AE energy increases exponentially with the increase of loading step, and the growth process can be divided into gentle period, acceleration period, and surge period. The mesoscale fracture damage calculation based on the fractal dimension can be utilized for quantitatively evaluating the spatial distribution characteristics of mesoscale fracture, which provides a new way to study the law of rock damage evolution.

1. Introduction

Because of the long-term influence of various geological processes, rock mass is cut into each other by different directions and different sizes of structural planes, forming discontinuous bodies with special structures, which leads to the formation of complex mesoscopic structures, and its failure mechanism will be more complicated [1–4]. In the process of rock failure, deformation problems such as crack initiation, shear zone formation, and stress concentration area distribution are closely related to its internal meso-structured. The heterogeneity of rock and the geometric distribution characteristics of joints with different dip angles have a vital effect on macroscopic failure mode and mesoscale damage evolution process of rock. Therefore, studying the macroscopic failure mode and mesoscale damage evolution process has important theoretical significance for revealing the macroscopic nonlinear mechanical behavior and damage mechanical properties of the jointed sandstone fracture process.

In recent years, scholars at home and abroad have never stopped the research on the cutting direction effects of joint on failure mode and damage evolution law of rock masses and have achieved rich results. Lou et al. have carried out a detailed study of the interrelatedness of joint dip angle with failure modes and shale strength by numerical simulation

experiments [5]. Yang et al. examined the joint inclination impacts as well as spacing on the fracture effect of sandstone and proposed a calculation model for joint rock failure [6]. Reik et al. conducted true triaxial compression tests on jointed rock mass specimens and studied the effects of joint direction and intermediate principal stress on specimens' compressive strength [7]. Sun et al. performed triaxial and uniaxial compression tests on jointed rock specimens through laboratory experiments and systematically analyzed the internal relationship between mechanical parameters such as elastic modulus and joint inclination angle [8]. Qian et al. studied the mechanical response and damage process of joint rock mass under stress wave [9]. Wasantha et al. carried out uniaxial compression on cement mortar joint specimens, showing that all the compressive strength was affected by trace length, inclination angle along with joint position [10]. Morteza et al. have studied the effect of joint direction and spacing on the macroscopic rupture of joint rock mass [11]. As' habi and Lakirouhani studied the peak strength and damage pattern of the joint rock by numerical simulation [12]. However, Liang et al. presented that mechanical process of rock fracture has self-similarity, and its failure has fractal characteristics. Stress in process of loading determines the fractal dimension of its damage [13]. There have been many research results on the relationship between fractal of the mesostructure of the rock and its compressive strength [14, 15]. Zhao et al. studied the propagation process of rock cracks through rock mechanics experiments and established a rock fractal damage constitutive model based on fractal theory [16]. Li et al. used numerical simulation methods to study the failure and fractal characteristics of rock in uniaxial compression tests [17]. Zhang et al. used physical tests and numerical simulation to study the association among fractal characteristics of cracks' geometrical distribution along with their mechanical properties after the rock failure finally in uniaxial compression tests [18].

Even though the above-mentioned research findings provide valuable points of reference for better understanding the damage of a jointed rock mass as well as mechanical properties at macroscopic scale, only a few researches have investigated, at the mesoscale, the local failure caused by an uneven stress distribution resulting from meso inhomogeneity of rock mass. While rock masses have mechanical characteristics and failure modes, their mesostructure is strongly connected to these qualities and failure modes; that is, macroscopic mechanical properties along with fracture processes of a rock mass are dependent on the materials' mesoscale behavior as well as mesostructure. By properly representing the mesostructure of the rock in the mesoscopic mechanical model, it will be possible to gain a better understanding of the failure mechanism and damage evolution process of the rock.

For this reason, this paper utilizes DIP technology for characterizing the real mesostructure of sandstone and combines it with the rock fracture process analysis system (RFPA2D) to establish a real mesostructure numerical model considering jointed sandstone with different inclination angles. Macroscopic mechanical characteristics and damage evolution of 7 groups of jointed sandstone with different dip angles under uniaxial compression are simulated, and the influence of mesostructure on macroscopic mechanical behavior and damage evolution of jointed sandstone with various dip angles is analyzed. Based on fractal theory, distribution of acoustic emission, the damage evolution, and the fractal characteristics of failure mode in the rock fracture process are deeply discussed.

2. Regional Geological Characteristics

The "Golden Triangle" of Yunnan, Guizhou, and Guangxi is a part of the Youjiang Basin that lies on the southwest edge of the Yangzi block. Near about 50,000 square kilometers area is covered by it and it extends approximately 400 kilometers east to west (Figure 1(a)).

In addition to being one of the most significant gold resources on the planet, Carlin-type gold deposits are also the world's primary source of gold. This kind of deposit is distinguished by the fact that the ore is housed in sedimentary rocks and that the gold is fine-grained and dispersed throughout [19–21]. The Lannigou gold deposit in the "Golden Triangle" is the world's largest Carlin-type gold deposit. In terms of geology, this is a classic fault-controlled deposit [22]. The Bianyang Formation, Niluo Formation, and Xuman Formation are the most exposed strata in the mining region. Terrigenous clastic turbidite is the dominant lithology that is composed mostly of calcium-bearing sandstone, mudstone, and siltstone from deep-water basins. Faults regulate the morphology of the ore body, and the ore body is mostly concentrated along the northwest-trending fault F3 and where it meets with the northeast-trending fault F2. A variety of calcareous fine-grained mudstones and sandstones, ranging in age from the Xuman Formation to the Bianyang Formation, are responsible for the mineralization of the region's ore (Figure 1(b)).

The sandstone cores in the F3 fault fracture zone of the Bianyang Formation were selected for high-resolution CT scanning (Figure 2) and X-ray mineral diffraction analysis; the sampling locations are shown in Figure 1(b).

Using an X-ray diffractometer, the mineral composition of sandstone can be calculated, as seen in Table 1. Table 1 shows that quartz is the most abundant mineral in sandstone, accounting for 50.9 to 62.9% of the total mineral composition. In the sandstone samples, illite is the most abundant clay component, followed by mixed layer illite-montmorillonite (6 percent-17 percent), with a small amount of chlorite (3 percent -28 percent) and kaolinite. Therefore, results obtained from the test show that samples are primarily composed of brittle minerals for example quartz.

3. Finite Element Method for Rock Failure Process

3.1. Digital Image Characterization of Sandstone Mesostructure. DIP technology identifies the spatial distribution and geometric shape of the mesocomponents of materials based on variations in gray-scale value and color, rather than on the basis of their physical properties. To

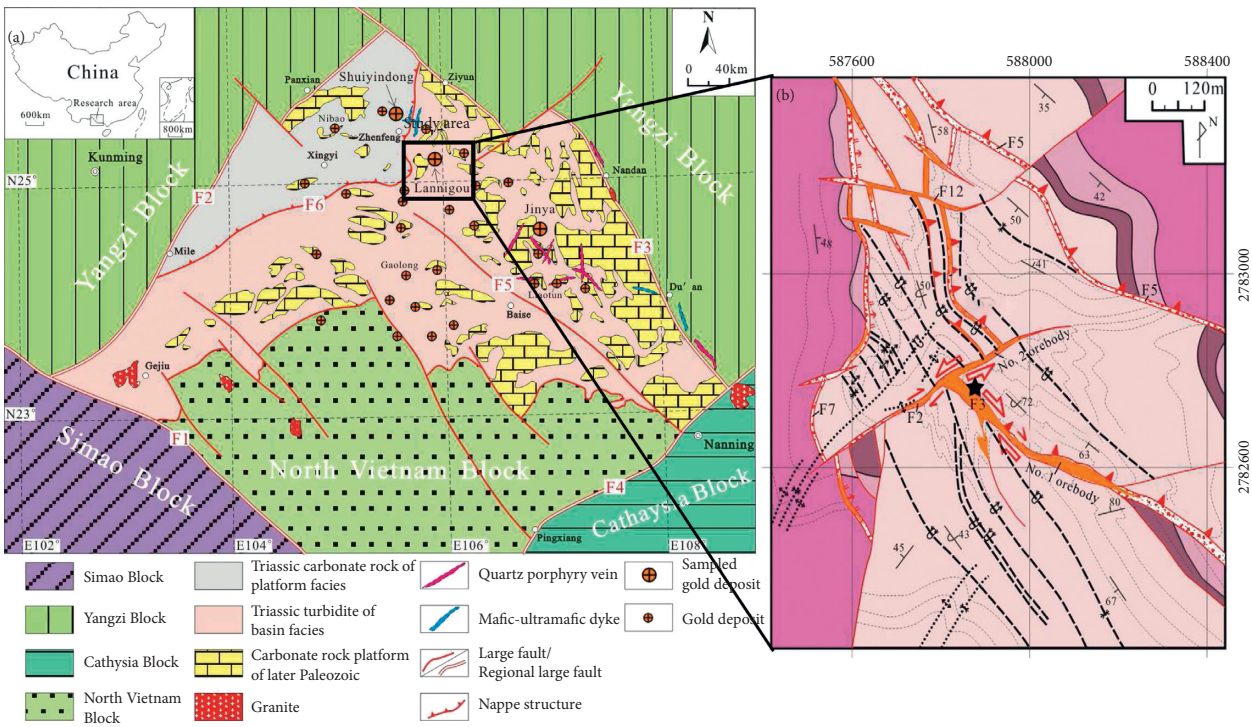

Figure 1: (a) Regional geological map of the Yunnan-Guizhou-Guangxi "Golden Triangle" region. (b) Schematic geological map of the Jinfeng gold deposit in Guizhou with the sampling locations.

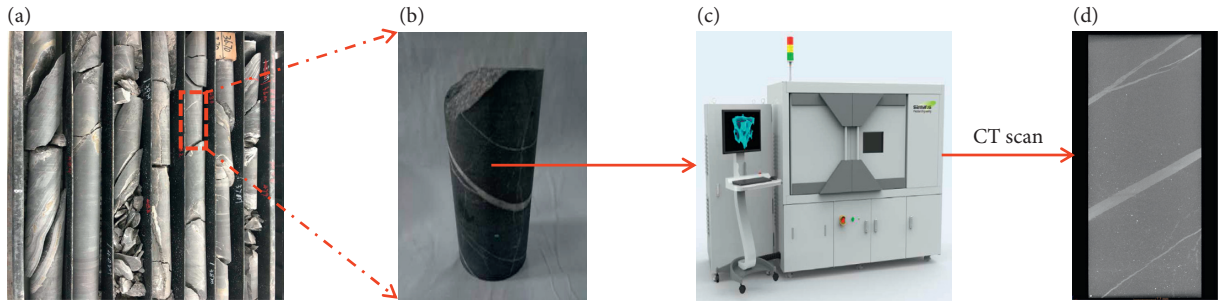

Figure 2: CT scanning process of jointed sandstone. (a) Core box, (b) sandstone sample, (c) nanovoxel-3503E, and (d) CT slice.

Table 1: Characteristic parameters and mineral compositions of sandstone samples.

Sample	Formation	Mineralogical composition (%)						Clay composition[a] (%)			
		Quartz	Feldspar	Calcite	Pyrite	Iron dolomite	Siderite	I/S	I	K	C
1	T_2by	60.5	1.3	13.4	3.5	5.0	0.4	11	89		
2	T_2by	53.5	2.8	0.2	2.5	6.7	0.7	6	91		3
3	T_2by	62.9	0.7	10.5	4.7	9.7	0.3	17	79		4
4	T_2by	50.9	29.6			7.8	3.1	8	37	28	27
5	T_2by	58.2	25.6	0.5	0.3	2.9	1.4	10	32	30	28

[a]I, Illite; k, Kaolinite; I/S, I/S mixed layer; C, Chlorite; S, Smectite.

evaluate the segmentation thresholds for different media within rock based on brightness and color, this technique is utilized. Once the segmentation thresholds are determined, the technique is utilized for classifying the image into various media, thus generating an image that characterizes the nonuniformity of material [23]. Tianjin Sanying Company performed high-resolution CT scanning, which resulted in the CT slice shown in Figure 3. This is a true color, 24 bit sandstone image with calcite-filled joint that has been processed. Sandstone is the dark-colored substance, and calcite is the light-colored material. The image has a resolution of 500 × 500 pixels, and the real dimension of the image

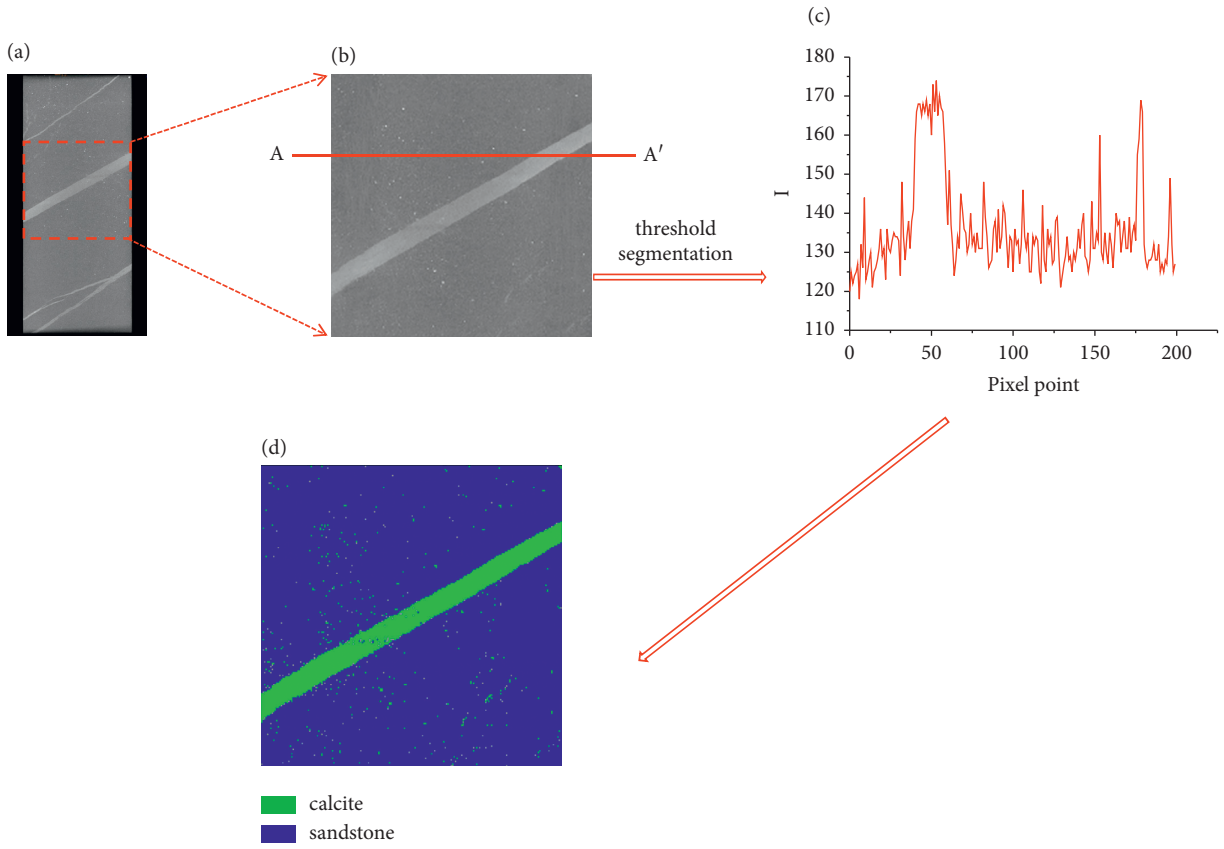

FIGURE 3: Digital image processing of jointed sandstone. (a) CT slice, (b) scan line AA′, (c) variation along I scan line AA′, and (d) threshold-segmentation characterization image of sandstone.

is 50 mm × 50 mm. In order to detect the color change, multithreshold segmentation by analyzing the variation in values of intensity (I) in the HIS (Hue, Saturation, and Intensity) color space, image processing to stretch contrast in order to increase the tonal distinction between the features was performed [23, 24]. Figure 3 depicts the location of the scan line AA′ as it moves through an image, and Figure 3 depicts plot of how the I value changes as scan line AA′ goes through the image. Many experiments in the image *J* software were conducted to determine the segmentation threshold that was determined to be 150 by comparing the mineral medium through which the scanning line travels with the change in the curve. This results in a two-section I value, ranging from 0 to 150 (sandstone) and 150 to 255 (calcite), indicating that the test sandstone sample's internal mesoscopic medium can be divided into two categories as per the I value distinction. Figure 3 is a characterization image obtained after image processing of Figure 3. According to Figure 3, the characterization imagery obtained from threshold segmentation can show the shape and spatial distribution of calcite in the sandstone sample more precisely.

3.2. Constitutive Relationship for Damage on the Mesoscopic Scale. As per the strain equivalence assumptions, in RFPA2D, ω (damage variable) is described as a change in elastic modulus [25]. The constitutive connection following material damage as a result of an external force may be described as follows [26, 27]:

$$E = (1 - \omega)E_0, \tag{1}$$

where damage variable is represented by ω and undamaged and damaged material's elastic modulus is represented by E_0 and E.

Because sandstone's compressive strength is significantly higher as compared to its tensile strength, we utilize the Mohr–Coulomb strength criterion as the criterion for element failure, with the tensile criterion serving as the failure criterion. The constitutive association of a mesoscopic element under uniaxial tension is seen in Figure 4 (tension or compression). Primarily the stress-strain curve is linearly elastic, whereas no evidence is found for any structure damage. It is the meso element that suffers brittle breakage after it has undergone the maximum tensile strain. Brittle rocks are vulnerable to tensile-induced failure, which is the most common kind of failure [28]. If tensile stress surpasses the element's tensile strength ft, according to primary damage criterion, damage occurs. The following is the expression for the tensile damage function [29]:

$$F^{-}(\sigma) = \sigma_3 + f_t = 0, \tag{2}$$

where principal stress vector is represented by σ. The constitutive connection of the mesoscopic element under

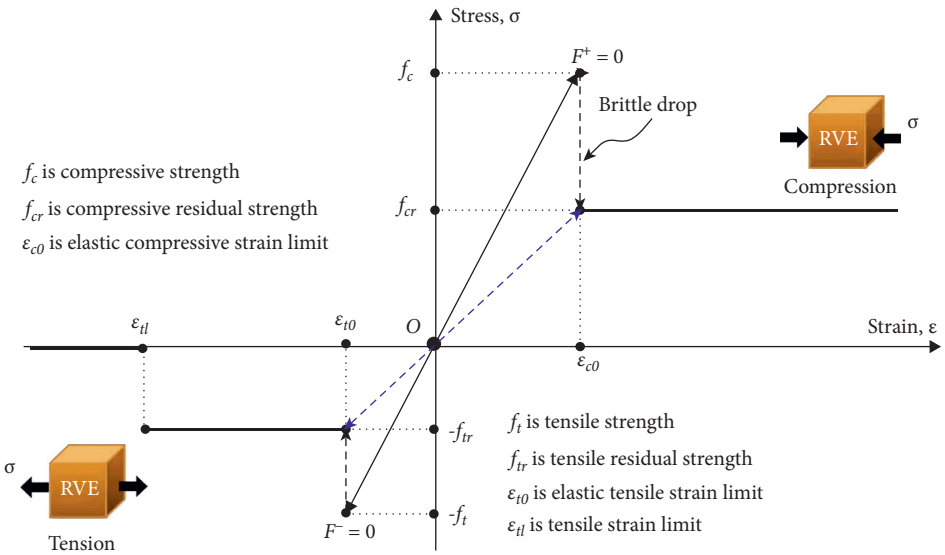

Figure 4: Constitutive association of elastic damage of mesoelement.

uniaxial tension can be stated as seen in the third quadrant of Figure 4 [30]:

$$\omega = \begin{cases} 0, & \varepsilon_{t0} \le \varepsilon < 0, \\ 1 - \dfrac{\lambda \varepsilon_{t0}}{\varepsilon}, & \varepsilon_{tl} \le \varepsilon < \varepsilon_{t0}, \\ 1, & \varepsilon \le \varepsilon_{tl}, \end{cases} \tag{3}$$

where λ represents the mesoscopic element's residual intensity coefficient, described as $f_{tr} = \lambda f_t$ (where mesoscopic element's uniaxial tensile strength is given by f_t, whereas f_{tr} is the residual strength at the element's initial tensile failure), and element's ultimate tensile strain is given by εtl. When the element's uniaxial tensile strain goes to ultimate tensile strain, then the element goes to tensile fracture state, i.e., complete failure. Ultimate strain coefficient is given by η, particularly characterized by $\varepsilon tl = \eta \varepsilon t0$. $\varepsilon t0$ is tensile strain corresponding to elastic limit that can be named as tensile failure strain threshold, which is calculated as [31]

$$\varepsilon t0 = \frac{-ft}{E_0}. \tag{4}$$

When a mesoscopic element is exposed to uniaxial compression, as illustrated in the first quadrant of Figure 4, the Mohr–Coulomb criteria for damage are used as the second criterion, which defines element damage under compressive or shear stress conditions [30]:

$$F^+(\sigma) = \sigma_1 - \sigma_3 \frac{1 + \sin\phi}{1 - \sin\phi} - fc = 0, \tag{5}$$

where friction angle is given by ϕ, principal stresses is given by σ_1 and σ_3, and uniaxial compressive strength is given by fc. ε element's damage variable under uniaxial compression may be given as [32, 33]

$$\omega = \begin{cases} 0, & \varepsilon < \varepsilon_{c0}, \\ 1 - \dfrac{\lambda \varepsilon_{c0}}{\varepsilon}, & \varepsilon \ge \varepsilon_{c0}, \end{cases} \tag{6}$$

where the coefficient of residual strength is given by λ, described as $ftr/ft = fcr/fc = \lambda$, whereas at elastic limit compressive strain is given by $\varepsilon c0$, which can be determined as [32, 33]

$$\varepsilon c0 = \frac{fc}{E_0}. \tag{7}$$

3.3. Establishment of the Numerical Model. This research makes use of DIP techniques in conjunction with finite element modelling. In FEM, study objects should be organized into several small grid elements. Given that digital image is made up of pixels that are organized in rectangle, where every pixel has the size of a small square, thus, the pixel may be considered as finite element mesh in the following way (Figure 5). The entire image of characterization can be transformed into several end element grids according to which the material parameters of every material composite are allocated to the image according to color and the uniform coefficients of the different components are added to the numerical model.

The numerical simulation in this work is carried out utilizing the rock failure procedure analysis system RFPA2D that is capable of simulating the mesoscopic fracture progression as well as the whole process of rock fracture [31]. In the numerical computations, we use the assumption that mechanical characteristics of calcite as well as sandstone's matrix components follow the Weibull distribution function [34], which takes into consideration the heterogeneity of the material:

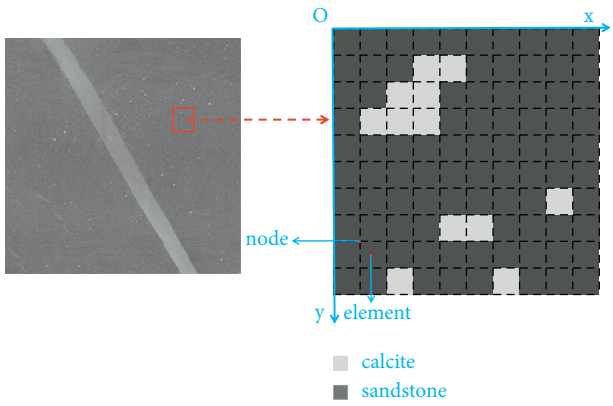

Figure 5: Digital image of sandstone and its finite element mesh model.

$$f(u) = \frac{m}{u_0}\left(\frac{u}{u_0}\right)^{m-1} \exp\left(-\frac{u}{u_0}\right)m, \tag{8}$$

where variables, for example, strength properties, Poisson's ratio, Young's modulus are given by u; the corresponding mean value is represented by u_0, where m describes the $f(u)$ shape, signifying the heterogeneity degree that can be called as heterogeneity index, and $f(u)$ is the material elements' statistical distribution density of mechanical properties. The inhomogeneity of sandstone and calcite is measured in this model, whereas Monte-Carlo technique is utilized for assigning the mesoelements' mechanical parameters [35, 36].

Table 2 shows the mechanical parameters of mesomedia inside the sandstone [37]. The actual size of the numerical model is 50 mm × 50 mm, the mechanical loading diagram is shown in Figure 6, the displacement compression loading control is adopted in axial direction, and planar stress was assumed. The initial displacement is 0.001 mm, and single-step increment is 0.001 mm, loading until the specimen failure.

To study the sandstone's mechanical properties with distinct dip angles and the mesoscopic inhomogeneity effects on the macroscopic sandstone fracture caused by the size, distribution along with shape of the calcite-filled joints is necessary to keep the basic medium of the image untouched irrespective to dip angle. To do this, the frames from the same section of a two-dimensional micro-CT image are clipped from a squeeze of 50 mm × 50 mm at various angles. The square center is fixed and digital images are recorded at 15° reverse clockwise, with a total of 7 images. Figure 7 shows the digital images' azimuth angles "are $\alpha = 0°$, $\alpha = 15°$, $\alpha = 30°$, $\alpha = 45°$, $\alpha = 60°$, $\alpha = 75°$, and $\alpha = 90°$, where α is the angle" between the horizontal direction and calcite-filled joint.

4. Results

4.1. Mechanical Properties of Sandstone under Uniaxial Compression. The simulation results of the specimen at $\alpha = 45°$ are selected to analyze the distribution characteristics of the stress. Figure 8 represents the elastic modulus distribution and principal stress in specimen when $\alpha = 45°$ at the initial loading stage. Due to heterogeneity of rock mesostructure, the brightness of different areas in the picture has a certain difference. Compared with the elastic modulus diagram, it is found that the internal stress distribution of the specimen filled with calcite veins is inhomogeneous, at the critical surface (weak structural surface) between calcite veins and sandstone, and it has higher brightness and significant stress concentration distribution, which indicates that the greater the brightness, the greater the stress. This shows that, in sandstone, the presence of calcite veins and mesostructure's heterogeneity have an important influence on the distribution of stress.

Table 3 shows the joints' elastic modulus and peak strength with distinct inclination angles. As demonstrated in Figure 9, there is clear anisotropy of the compressive strength and elastic module of jointed sandstone and variations in U-form as joint inclination increases. This might be because of inherent anisotropy of the sandstone and poor cementation of the calcite due to the arrangement of matrix and minerals. This conclusion is in good agreement with the study conclusions of Wang et al. [38] and Sun et al. [8], and it also shows that the results of numerical simulation are reliable. The compressive strength of sandstone reaches the maximum when $\alpha = 0°$, which is 81.47 MPa; when $\alpha = 60°$, it reaches the minimum, which is 55.68 MPa. If the angle of inclination for the joint is 60°, the friction angle of the specimen is larger than the internal angle. When the exemplar is squeezed, the shear strength on the contact surface between calcite along with sandstone, which is the explanation for the discrepancy, is larger than the overall frictional power and the cohesive force. This will lead to a shear failure alongside calcite-sandstone contact, with a very low compressive strength. When the azimuth angle is 90° or 0°, this test component will no longer move over the surface, thereby substantially improving compressive strength. As shown in Figures 9 and 10, due to the influence of sandstone mesostructure, the compressive strength and macroscopic failure mode of jointed sandstone reflect significant anisotropic characteristics.

In acoustic emission diagrams, white color in Figure 10 shows compressive shear damage created by element during the current loading stage and yellow denotes tensile damage at the current step, while black elements indicate all the damage.

As shown in the figure, this is observed when $\alpha = 0°$. On the sample's left side, the cracks as well as calcite veins start to crack at about 45°, the accumulation of tensile failure resulting in the stable expansion of the cracks, which eventually leads to the penetration of cracks and formation of oblique Z-shaped failures. When $\alpha = 15°$, the cracks started to sprout along the left end of the specimen as well as spread steadily perpendicularly to the calcite vein. With the increase of axial stress, a large amount of tensile failure occurred inside the specimen and was accompanied by a small amount of shear failure, resulting in crack expansion and penetration, eventually forming M-shaped failure. When $\alpha = 30°$, on the left side of the specimen, the cracks begin to crack along the weak surface of calcite vein and

Table 2: Mechanical parameters of sandstone specimen.

Material	Elastic modulus (GPa)	Compressive strength (MPa)	Poisson ratio	Compression-tension ratio	Internal friction angle/(C°)
Sandstone	108.2	118	0.16	14	35
Calcite	80.5	101	0.30	11	30

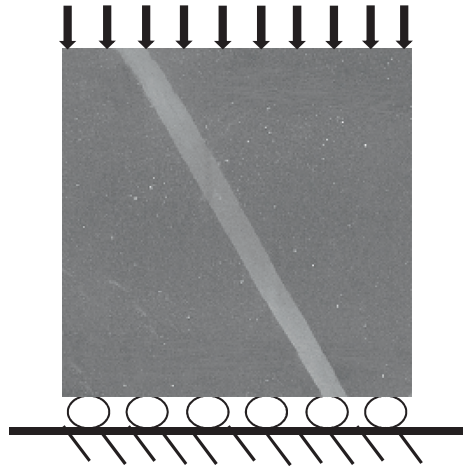

Figure 6: Mechanical loading diagram of the numerical model.

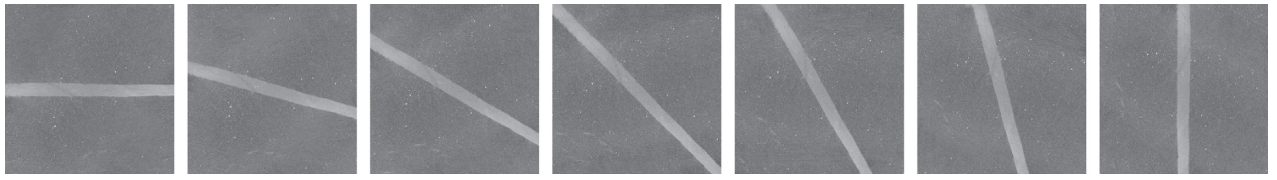

Figure 7: Digital image of jointed sandstone with distinct inclination.

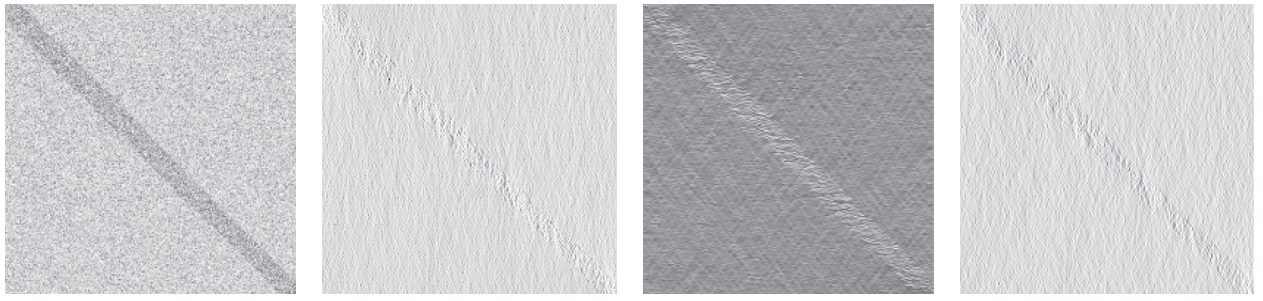

Figure 8: Distribution of principal stress and elastic modulus of the specimen at initial loading. (a) Elastic modulus, (b) maximum principal stress, (c) minimum principal stress, and (d) maximum shear stress.

sandstone and expand in the calcite vein. With the increase of axial stress, the cracks change the expansion direction and increase steadily along the maximum principal stress direction, eventually forming V failure. The cracks start along the middle of the calcite vein and expand along the two ends of the calcite vein when $\alpha = 45^{\circ}$. With the increase of stress, the veins of calcite are penetrated along with a macroscopic shear band created inside the specimen, which causes the specimen to produce linear failure. When $\alpha = 60^{\circ}$, cracks start to sprout at the calcite veins' lower end and expand along calcite veins. As stress increases, the crack increases steadily along the direction of maximum principal stress, a macroscopic shear zone is formed due to a large amount of tensile failure inside the sample, and finally N shape failure is formed. When $\alpha = 75^{\circ}$, the cracks start at the calcite vein's upper end and expand through calcite vein. As stress

Table 3: Simulation results of sandstone compressive strength and elastic modulus.

Joint inclination (°)	Compressive strength (MPa)	Elastic modulus (GPa)
$\alpha = 0^{\circ}$	81.47	88.17
$\alpha = 15^{\circ}$	77.96	86.63
$\alpha = 30^{\circ}$	72.51	85.31
$\alpha = 45^{\circ}$	65.71	65.71
$\alpha = 60^{\circ}$	55.68	50.33
$\alpha = 75^{\circ}$	71.95	84.68
$\alpha = 90^{\circ}$	76.16	89.66

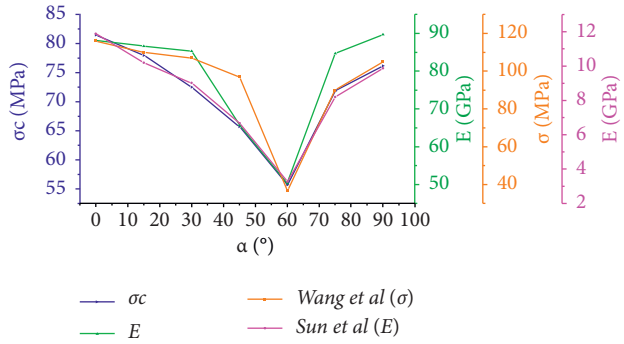

Figure 9: Elastic modulus and compressive strength of jointed sandstone with different dip angles.

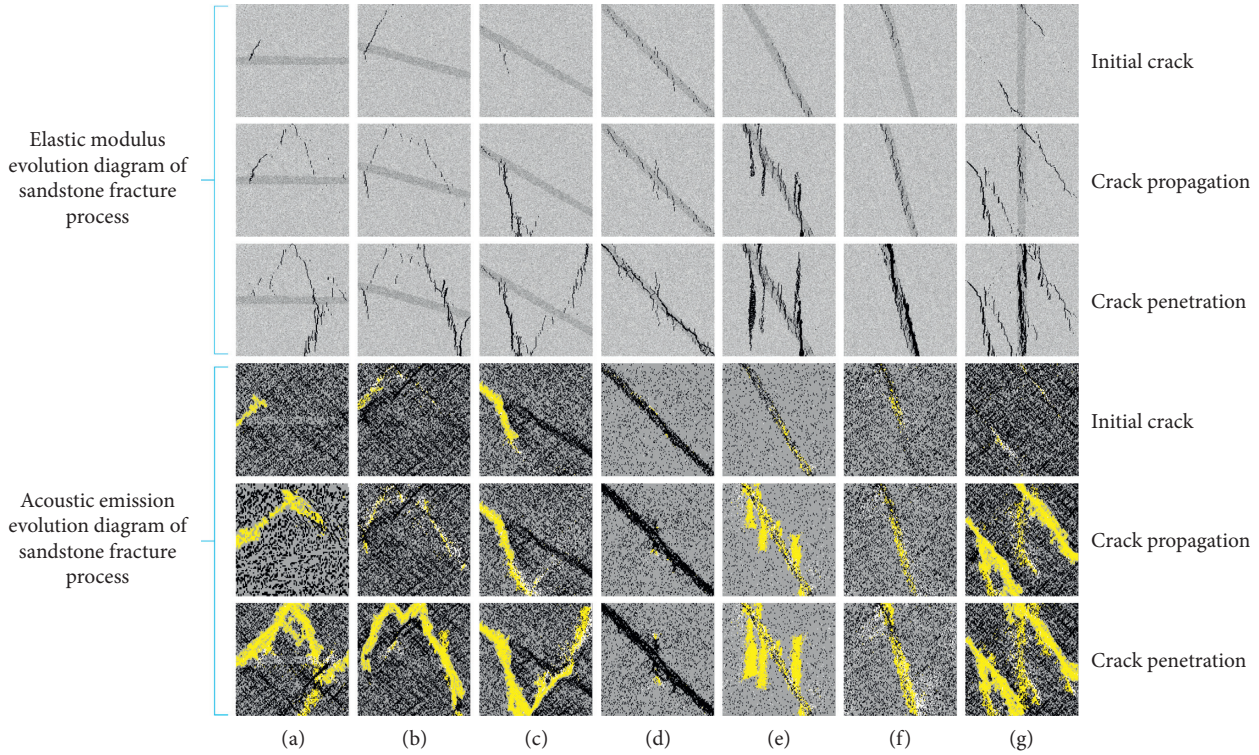

Figure 10: Crack propagation characteristics and fracture process evolution diagram of jointed sandstone with different dip angles.

increases, the veins of calcite are penetrated, causing the specimen to eventually fail and form a linear failure. When $\alpha = 90^{\circ}$, the initiation of cracks starts at both ends of calcite veins. As stress rises, 2 key cracks occur on both sides of the calcite vein and 2 key cracks are about 30° from the calcite vein, and as loading progresses, a large amount of tensile failure occurs inside the sample, which causes calcite veins to penetrate and form an oblique N-shaped failure.

From the acoustic emission evolution diagram, it can be seen that the elements are mostly tensile failure (yellow), and the macroscopic shear bands created by the specimen failure are connected mostly by tensile failure elements. This is because there is a stress concentration zone in compressed rock, the calcite veins filled in the sandstone are weak structural planes, and damage and failure occur first when they are mechanically loaded. Stress values will first exceed rock strength at specific local position and cause damage; this is the main impact of stress concentration which causes variations in the evolution of damage as well as mechanical failure behavior of distinct mesostructures.

4.2. Acoustic Emission Evolution Characteristics. In rock deformed under load, acoustic emission is a measurable response that occurs every time a microfracture occurs. This is a useful instrument for investigating the development of internal damage in rock, since this is caused by the fast discharge of sound energy during microcrack formation and growth. Because RFPA2D shows that the failure of every element represents the source of an acoustic event and because sample element failure will release the stored elastic energy throughout deformation process, RFPA2D may be used to mimic acoustic emission activities [23]. The evolution of acoustic emission process describes the whole rock fracture process, making it feasible to evaluate the fracture evolution law while the rock is fractured by counting the number of damaged components and the energy released by the resulting acoustic emission. Figure 11 is a trend diagram of load-displacement, AE energy, and accumulated AE energy with loading steps under different loading conditions.

The obvious difference of acoustic emission counts in the failure process of jointed sandstone with different dip angles is related to the failure mode of the samples. Figure 11 clearly shows that loading step is directly proportional to stress. Although there is an evident stress reduction following the peak strength, there is still significant residual strength. All samples can be divided into three stages during the failure: elastic stage, failure stage, and yield stage. Since no element damage occurred at the loading initial stage, the AE count and accumulated AE energy were basically 0. With the continuous action of the axial compressive stress, when $\alpha = 90^{\circ}$, element damage appears first in the sample. AE energy is the elastic energy released under compression; this can be observed from the figure that AE energy gradually rises with the load rise and reaches the maximum near the peak strength. This is because the greater the load is, the more the elements are damaged, and the more the elastic energy is released. When $\alpha = 90^{\circ}$, two microcracks in sample sprout along the two ends of calcite vein (Figure 10), so the AE energy distribution is the densest, and internal damage is the most severe (Figure 11). Secondly, the AE energy distribution is relatively dense in the interval of $\alpha = 0^{\circ}45^{\circ}$ (Figures 11(a)–11(d))), and, finally, the distribution of AE energy is relatively sparse in the interval of $\alpha = 60^{\circ}$~75°(Figures 11(e)–11(f))). Accumulative AE energy increases exponentially with the increase of loading step, and the growth process can be divided into gentle period, acceleration period, and surge period. This is because gentle period is in the initial stage of loading, AE events are less, the AE signal is relatively weak, the stress is in the linear elastic stage, and no obvious cracks are generated. When acceleration period is reached, the cumulative AE events show a linear increase, there are more AE events, a large amount of elastic energy is suddenly released, the AE signal is strong, and cracks extend and expand rapidly. When stress reaches the peak, it enters surge period, sandstone sample suddenly is failure, and cumulative AE energy increases instantly and reaches the maximum.

5. Fractal Analysis of Mesoscale Damage of Sandstone

5.1. Images Fractal Analysis Based on Box Dimension. Mandelbrot proposed the fractal damage theory, analyzing as well as investigating various unstable, irregular, and extremely complex phenomena that occur in nature and are based on mathematical calculations. It has found widespread use in a variety of areas, including geology and nonlinear science [24, 39]. Specifically, in this work, we choose a self-similarity box dimension computation technique, which is described as follows [40, 41]:

$$Ds = \lim_{k \longrightarrow \infty} \frac{\lg N r_k(A)}{\lg 1/r_k}, \tag{9}$$

where self-similar fractal dimension of the damaged region is Ds, and the developed reducing sequence with element's square box size is r_k. The least number of grids necessary for covering the target set A with a square box of size r_k is $Nr_k(A)$.

This study aims to utilize box dimension to investigate the fractal of mesoscale failure element area of jointed sandstone with varying dip angles in order to better understand the failure mechanism. It is possible to determine the fractal dimension of the mesoscale failure element area of jointed sandstone with varied dip angles and different stresses at different stress levels. Figure 12(a) presents the binary image of mesoscale fracture evolution at different stress levels when $\alpha = 30^{\circ}$. In different areas, the density and coverage area of the failure element are different, the number of pixels covering the failure element area is different, and accordingly, the fractal dimension is also different. The author uses the box coverage technique for calculating fractal dimension of the failure element by using the number of pixels covered by damage element area, and the image resolution is 500 pixel × 500 pixel.

Figure 12(b) is the box covering various regions, which is dividing the mesoelement failure area into a small square grid with r_k side length (the length of each image pixel is described as 1 in this paper) and then counting the number Nr_k of all boxes comprising failure element region. A dichotomy is used to construct r_k in this paper. If the failure element distribution in this area satisfies the fractal features, a formula shows that "when the $r_k \longrightarrow 0$, $\lg Nr_k/\lg r_k \longrightarrow D$, the fractal dimension of the failure element field (acoustic

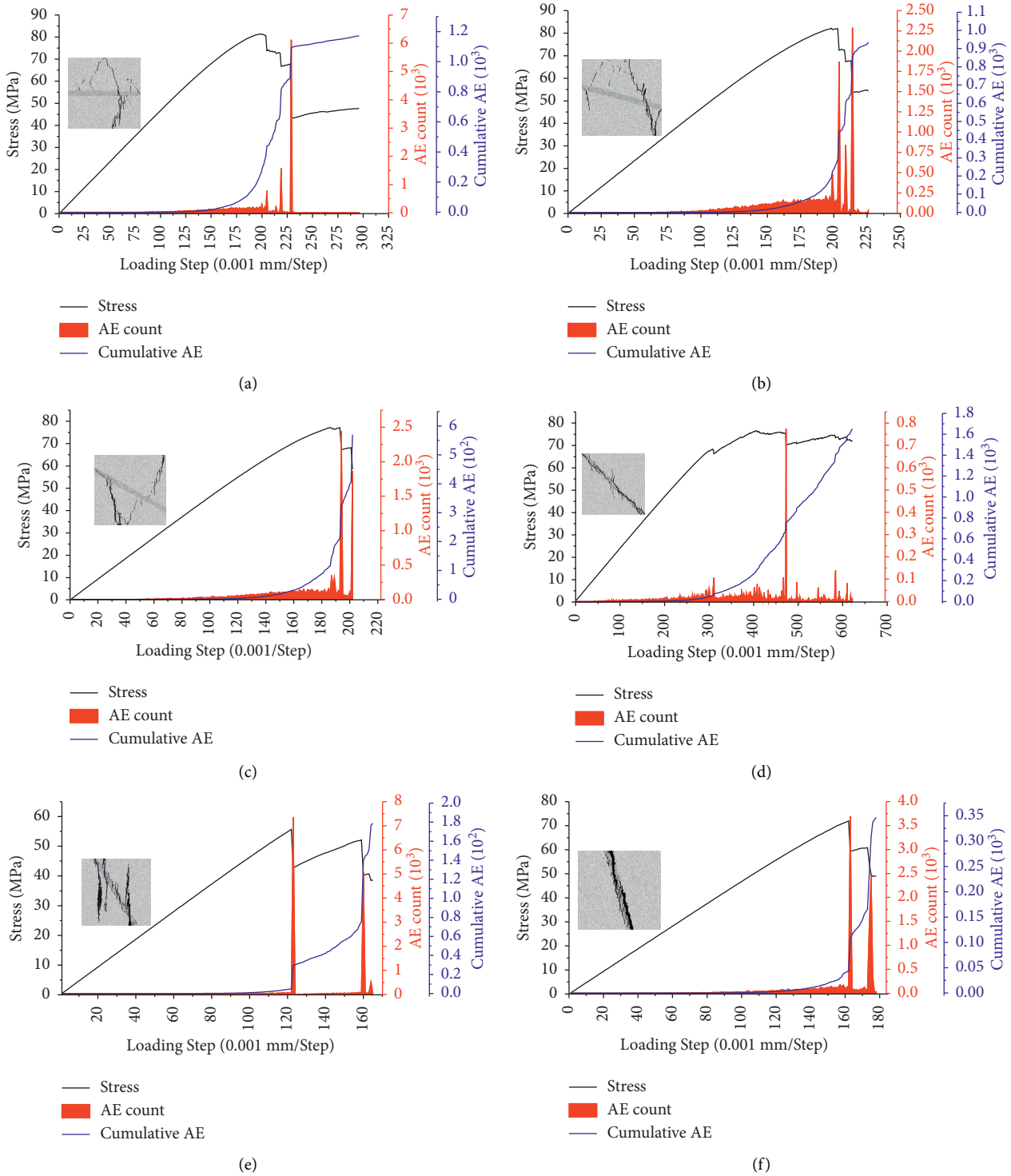

Figure 11: Continued.

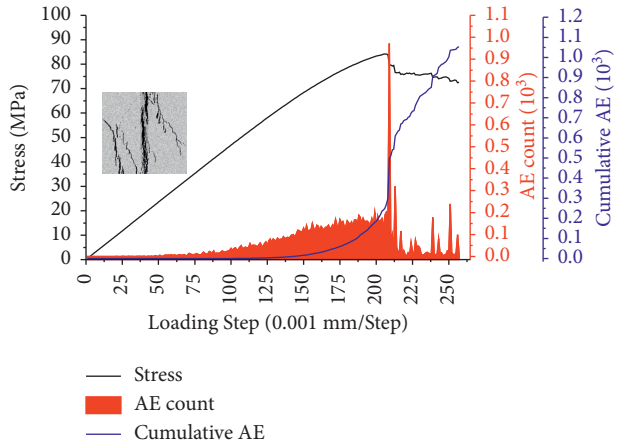

(g)

Figure 11: Trends of stress, AE energy, and cumulative AE energy with loading step at different azimuth angles. (a)–(g) represent specimens 0°, 15°, 30°, 45°, 60°, 75°, and 90°, respectively.

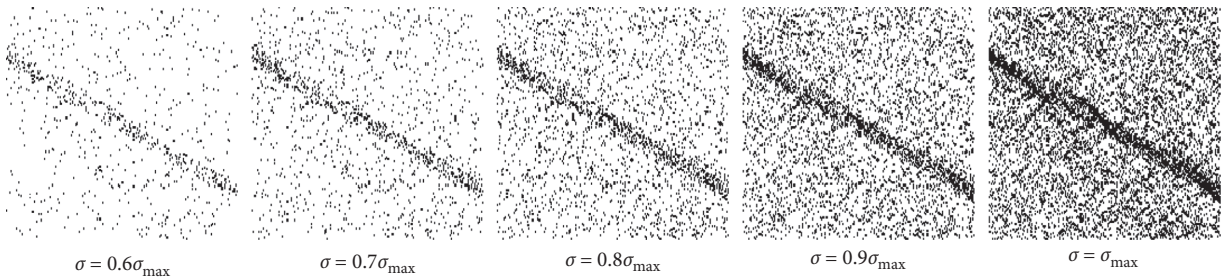

(a)

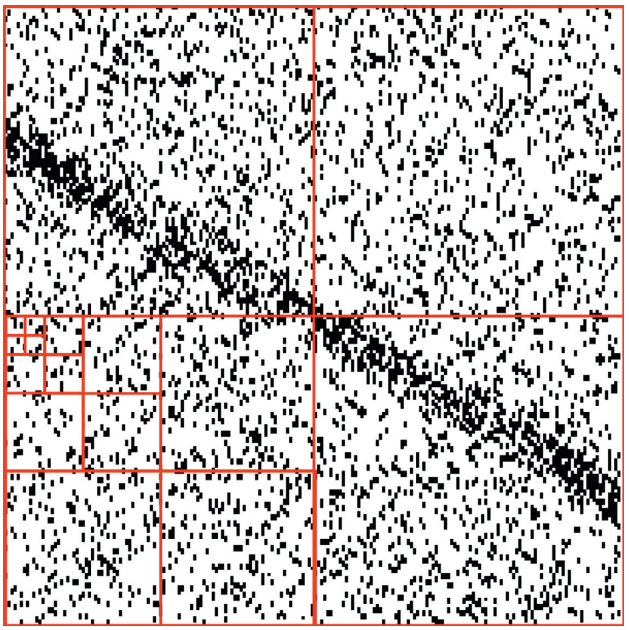

(b)

Figure 12: Schematic diagram of box dimension calculation for damage zone of sandstone mesoelement. (a) Binary image of damage evolution at different stress levels ($\alpha = 30°$). (b) Sketch for box dimension during rock failure process.

emission field) in this area is D. Hence, in the double logarithmic coordinate system, the data points ($\lg r_k$, $\lg Nr_k$) are linearly fitted by the least square method, and the straight line equation" can be found:

$$\lg Nr_k = D\lg r_k + b, \tag{10}$$

where D is the box counting dimension of the field of the failure element.

MATLAB programming is utilized to automatically mesh and statistically analyze the acoustic emission evolution image of a mesoscale rock failure and to determine the fractal dimension of the rock failure based on the aforementioned approach. The calculating procedure is depicted in Figure 13.

Whereas damage variable may be utilized to statistically characterize the progression of the microfracture, it is not reflective of the microfracture's spatial distribution and the results are limited. Xie has proven that rock failure procedure has fractal properties since a fracture begins [42]. Following this understanding, the fractal dimension of the acoustic emission field is used as the characteristic parameter for describing the mesoscale damage evolution of the rock. Not only the fractal dimension based on the acoustic emission field is able to quantitatively analyze the evolution process of the mesoscale failure of the rock, but also the damage evolution and macrodamage characteristics of the meso element in the material can be unified. The connection between the degree of destruction of the rock mesoscale fracture and the D fractal dimensional value of the "acoustic emission field" in specimen may thus be developed and stated as

$$\omega = \frac{D - D_0}{D^{\max} - D_0}, \tag{11}$$

where D is the fractal dimension of the damaged area of the mesoscopic element of the rock after stress loading, D_0 is the fractal dimension of the initial damage area of the mesoscopic element of the rock before stress loading, and $D^{\max}$ is the fractal dimension when the mesoscopic element of the rock reaches the maximum damage area.

The acoustic emission charts under different dip angles and corresponding levels of stress are analyzed using MATLAB. Figure 14 is a process of calculating the box dimension of the acoustic emission binary image, and Figure 15 is fractal fitting diagram of sample failure when stress level is 50% and $\alpha = 30^\circ$. The damage degree, acoustic emission energy values, and fractal dimensions of specimens at various stress levels are given in Table 4.

It can be observed in Figure 16 that the increase of the acoustic emission energy curve in each group of azimuth angles is relatively flat and the change trend tends to be consistent when the stress level is lower than 70%. The acoustic emission energy curve of the sample rapidly increases when the stress level is higher than 80% and reaches the maximum when $\alpha = 90^\circ$. When $\alpha = 15^\circ$ and $\alpha = 60^\circ$, the sample takes second place, and when $\alpha = 75^\circ$, the acoustic emission energy value of the sample is the minimum. Therefore, it shows that when $\alpha = 90^\circ$, the energy released by the sample failure after being loaded is the largest, and the ultimate damage is the most severe.

It can be seen from Figures 17 and 18 that under all azimuth angles, as per the continuous increase of the stress level, the fracture damage degree along with the fractal dimension continues to increase; the fractal dimension along with fracture damage degree has same changing trend. The fractal dimension of rock damage zone is positively correlated with load, and the rise of the fractal dimension is synchronized with the change of damage. The samples are in the elastic stage and the $Ds = 0$ when the stress level is 10%, which means that the samples are not damaged. The Ds of the specimen under all azimuth angles will increase rapidly when the stress level is lower than 30%. When the stress level is above 40%, with the increase in stress levels, the fractal and fracture damage of the samples is increased and trends are comparable. When $\alpha = 90^\circ$, the fractal sampling dimension value is at 100% and the fracture damage level is 0.90, both being the maximum. When $\alpha = 75^\circ$ and when 100% is stress level, the fractal sample dimension value is 1.52 and 0.76 is fracture damage degree, both of which are the minimum. As shown in Section 4.2, when $\alpha = 90^\circ$, the sample shows an oblique N-shaped failure, the final failure mode is the most complex whereas damage is the most serious; thus, rupture damage and fractal dimension are the largest. When $\alpha = 75^\circ$, the cracks initiated, expanded, and penetrated along the calcite veins, so the fracture damage and fractal dimension are the smallest. For specimens whose final fracture modes are V-shaped, oblique Z-shaped, inverted N-shaped, and M-shaped, the fractal dimension is between linear failure and oblique N-shaped. Thus, the larger the Ds, the more complicated the final failure mode, the greater the fracture damage degree, and the more severe the final damage of the specimen.

6. Discussion

6.1. Reliability Verification of Numerical Simulation Results. Since the above research is based on numerical simulation, to verify its reliability, the established numerical model needs to be verified. This section verifies its reliability by theoretical analysis; in Figure 19 is a mechanical model with a single joint, and β is the angle between joint and direction of the maximum principal stress. According to Mohr circle theory, the normal stress σ and shear stress τ acting on the joint surface are

$$\begin{cases} \sigma_\theta = \dfrac{1}{2}(\sigma_1 + \sigma_3) + \dfrac{1}{2}(\sigma_1 - \sigma_3)\cos 2\theta, \\ \\ \tau_\theta = \dfrac{1}{2}(\sigma_1 - \sigma_3)\sin 2\theta. \end{cases} \tag{12}$$

For specimens with single joints, the conditions for failure along the joints are

$$\sigma_1 \geq \sigma_3 + \frac{2\left(c_j + \left|\sigma_3\right|\tan \phi_j\right)}{\left(1 - \tan \phi_j \tan \beta\right)\sin 2\beta}. \tag{13}$$

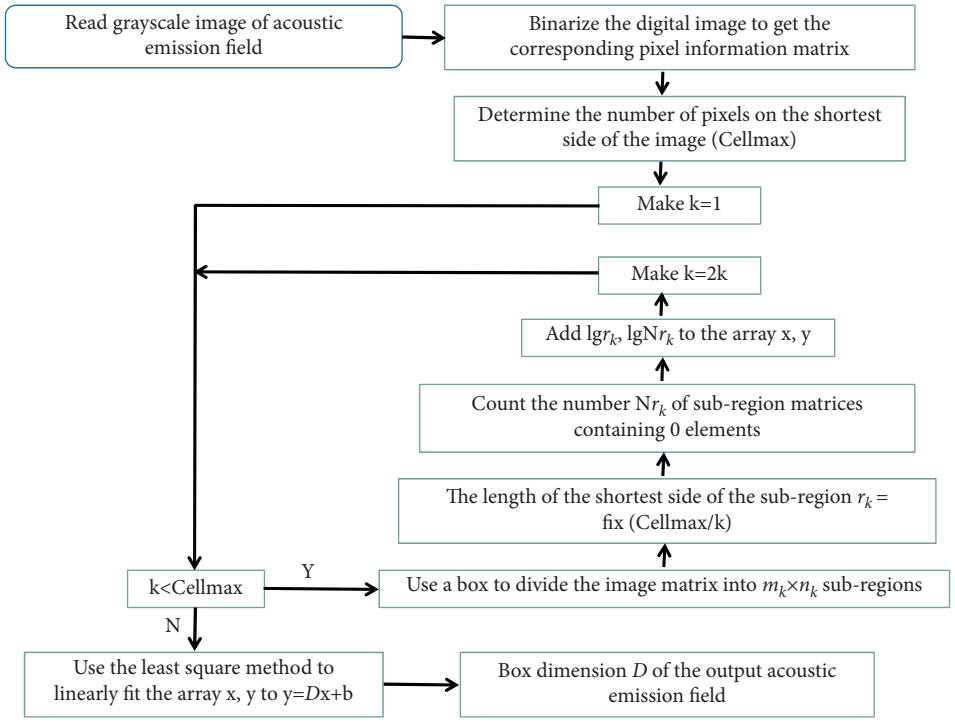

Figure 13: Calculation box dimension process of acoustic emission field based on MATLAB.

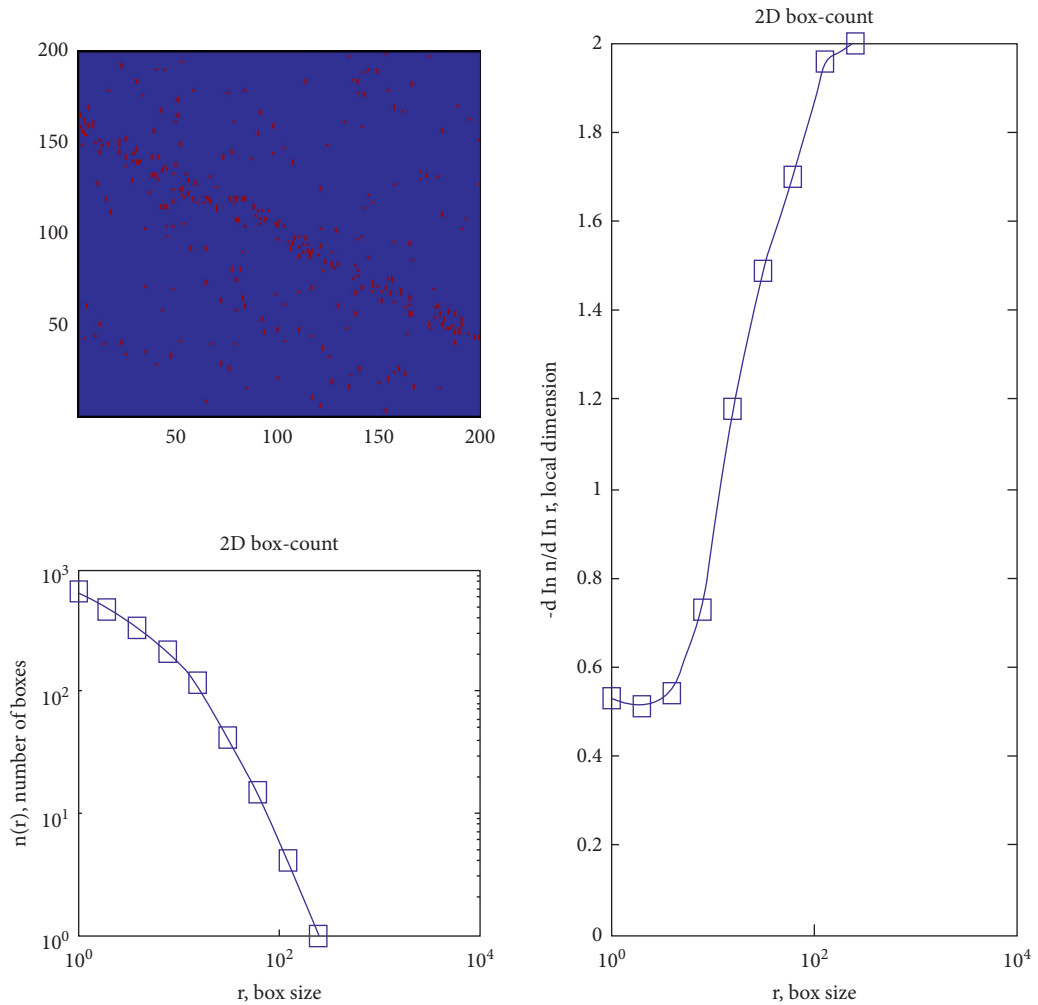

Figure 14: The calculation process of fractal dimension when the azimuth angle of the joint is 30° at stress level of 50%.

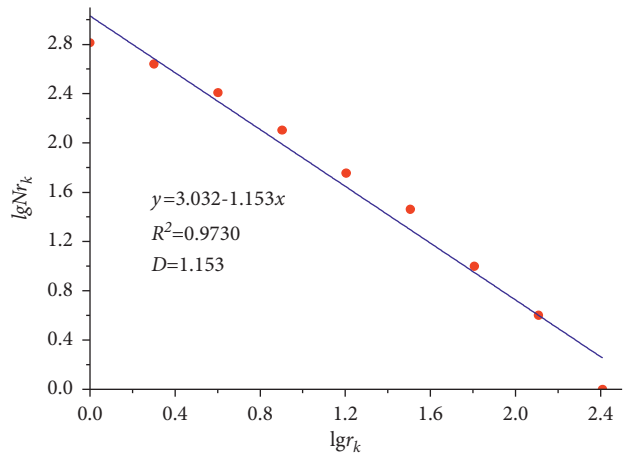

Figure 15: Fitting curve diagram of fractal characteristics of damage area when joint inclination is 30° (stress level is 50%).

Table 4: Values of fractal dimension, damage degree, and AE energy for sandstone samples under different stress levels.

Joint inclination		Stress level 10%	20%	30%	40%	50%	60%	70%	80%	90%	100%
	AE	0	2	4	6	18	41	76	93	132	254
$\alpha = 0^\circ$	D	0	0.29	0.57	0.91	1.17	1.36	1.51	1.62	1.71	1.79
	ω	0	0.145	0.285	0.455	0.585	0.68	0.755	0.81	0.855	0.895
	AE	0	1	4	4	17	33	70	108	118	187
$\alpha = 15^\circ$	D	0	0.26	0.66	0.94	1.17	1.34	1.50	1.63	1.72	1.782
	ω	0	0.13	0.33	0.47	0.585	0.67	0.75	0.815	0.86	0.891
	AE	0	1	1	10	14	35	50	84	103	115
$\alpha = 30^\circ$	D	0	0.37	0.63	0.93	1.153	1.35	1.47	1.59	1.68	1.76
	ω	0	0.185	0.315	0.465	0.577	0.675	0.735	0.795	0.84	0.88
	AE	0	1	4	8	21	31	66	97	136	365
$\alpha = 45^\circ$	D	0	0.39	0.58	0.85	0.97	1.12	1.28	1.39	1.42	1.53
	ω	0	0.195	0.29	0.425	0.485	0.56	0.64	0.695	0.71	0.765
	AE	0	2	3	5	14	18	22	42	51	77
$\alpha = 60^\circ$	D	0	0.28	0.52	0.88	1.13	1.25	1.37	1.45	1.58	1.73
	ω	0	0.14	0.26	0.44	0.565	0.625	0.685	0.725	0.79	0.865
	AE	0	2	4	9	16	29	44	67	103	155
$\alpha = 75^\circ$	D	0	0.36	0.56	0.78	0.88	1.04	1.16	1.30	1.42	1.52
	ω	0	0.18	0.28	0.39	0.44	0.52	0.58	0.65	0.71	0.76
	AE	0	1	6	14	15	39	80	117	144	189
$\alpha = 90^\circ$	D	0	0.49	0.64	0.94	1.18	1.37	1.52	1.64	1.73	1.80
	ω	0	0.245	0.32	0.47	0.59	0.685	0.76	0.82	0.865	0.9

In the formula, c_j, ϕ are the adhesive force and the joint surface's internal friction angle, angle between the joint, and σ_1 is given by β.

As per Mohr-Coulomb criterion, when rock model fails, there are

$$\sigma_1 = \sigma_3 k - 2c\sqrt{k}, \tag{14}$$

where $k = (1 + \sin\phi/1 - \sin\phi)$.

Under uniaxial compression ($\sigma_3 = 0$), formulas 12 and 14 can be simplified to

$$\begin{cases} \sigma_1 = \dfrac{-2c_j}{(1 - \tan\phi\ \tan\beta)\sin 2\beta}, \\ \sigma_1 = -2c\sqrt{k}. \end{cases} \tag{15}$$

Under uniaxial compression, the compressive strength of the model with joints is

$$\sigma_c = \begin{cases} \min\left\{2c\sqrt{k}, \dfrac{-2c_j}{(1 - \tan\phi\ \tan\beta)\sin 2\beta}\right\}, & (1 - \tan\phi\ \tan\beta) > 0, \\ 2c\sqrt{k}, & (1 - \tan\phi\ \tan\beta) < 0. \end{cases} \tag{16}$$

$(1 - \tan\phi\ \tan\beta) = 0.42265 > 0$; $k = 3$. The results show that the jointed model will fail along the joint surface under uniaxial compression. Figure 20 is a numerical simulation fracture process diagram of jointed sandstone. The initial cracks start along the calcite veins and propagate along both

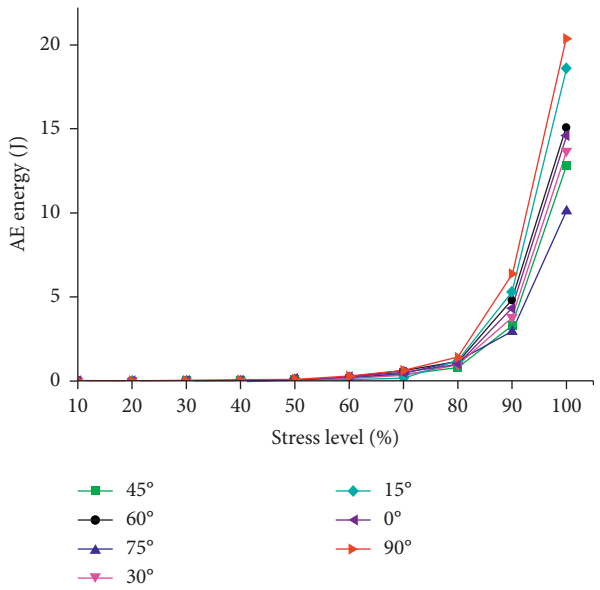

Figure 16: Relationship between distinct stress levels and AE energy.

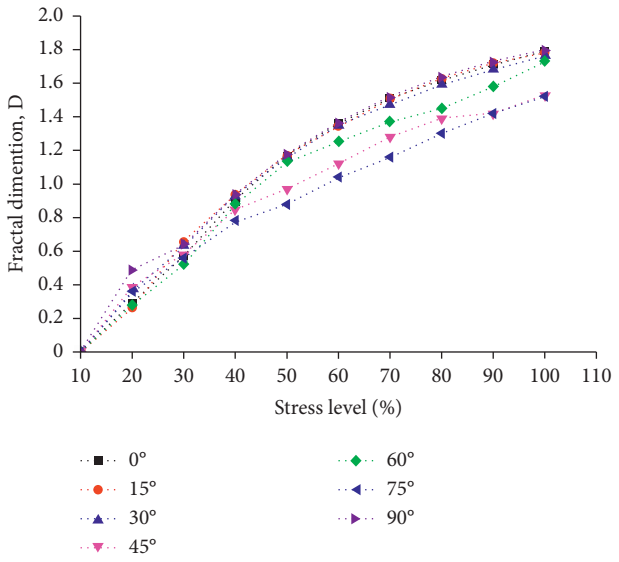

Figure 17: Relationship between distinct stress levels and fractal dimension.

ends of the calcite veins, and as stress increases, the veins of calcite are penetrated, and a macroscopic shear band is formed inside the sample, which causes linear failure. The numerical simulation results are consistent with the calculation results of the mechanical model, indicating that the numerical test results are highly reliable.

6.2. The Guiding Significance of Mechanical Behaviors. This study shows that the elastic modulus and compressive strength of jointed sandstone have obvious anisotropy, and they all present U-shaped changes as the joint inclination increases. This is constant with Sun et al. [8] along with Wang et al.'s [38] results. However, Wang et al. [38] and Sun et al. [8] only studied the macromechanical properties of rocks and did not consider the influence of rock mesostructure on its macromechanical behavior. Nevertheless, the stress distribution and failure mode of rock are closely related to its mesostructure, and the macroscale fracture process and mechanical properties depend on mesoscale behavior as well as the mesostructure of material. In this paper, the failure mode of jointed sandstone with different dip angle is studied based on the consideration of its mesostructure in the numerical model, and the outcomes demonstrate that the energy released by the fracture of $\alpha = 90^{\circ}$ is the largest, the final failure degree is the most severe, and internal damage is the most serious. Further, the more fully the rock is broken, the more complex the fracture mode is. In mining activities, it is necessary to fully understand its geological conditions and choose a position where the joint inclination is close to vertical for blasting. This will make the ore crush more fully, thereby improving mining efficiency.

6.3. Fractal Characteristics and Application of Box Dimension of Acoustic Emission Evolution Image. The fractal study shows that fractal dimension can characterize quantitatively the complexity of sandstone failure mode and the degree of fracture damage can quantitatively describe the degree of sandstone damage. Figure 15 shows that the correlation coefficient is $R^2 = 0.973$, which indicates that the damage evolution process of sandstone is fractal and the mesoscale fracture distribution has good self-similarity, and fractal dimension has high credibility, which is consistent with the study conclusion of Liang et al. [13]. However, the damage fractal of rock throughout loading is related to the stress [14, 15]. Zhao et al. studied the propagation process of rock cracks through rock mechanics experiments and established a rock fractal damage constitutive model based on fractal theory [16]. Zhang et al. used physical tests and numerical simulations to study the correlation between fractal characteristics of cracks' geometrical distribution along with their mechanical properties after the rock finally fails in uniaxial compression tests [18]. Rock failure is actually the process of cumulative damage development. If the fractal dimension of the damage that occurs during failure is calculated for rocks under various stress levels, the variation law of the fractal dimension in the process of damage evolution can be observed. However, the above studies only consider the variation in fractal dimension during a certain stage of the fracture process, and there has been little research on the entire process from initial damage to the final failure of the rock. Numerical simulation of the fractal characteristics of rock is usually based on the assumption that rock microstructure is randomly distributed, without considering the nonuniformity of rock.

In this study, through the development of a numerical model that takes into account the real mesostructure of rock, the authors investigated the fractal characteristics of acoustic emission under various stress levels. The results of the fractal research revealed that the material damage evolution

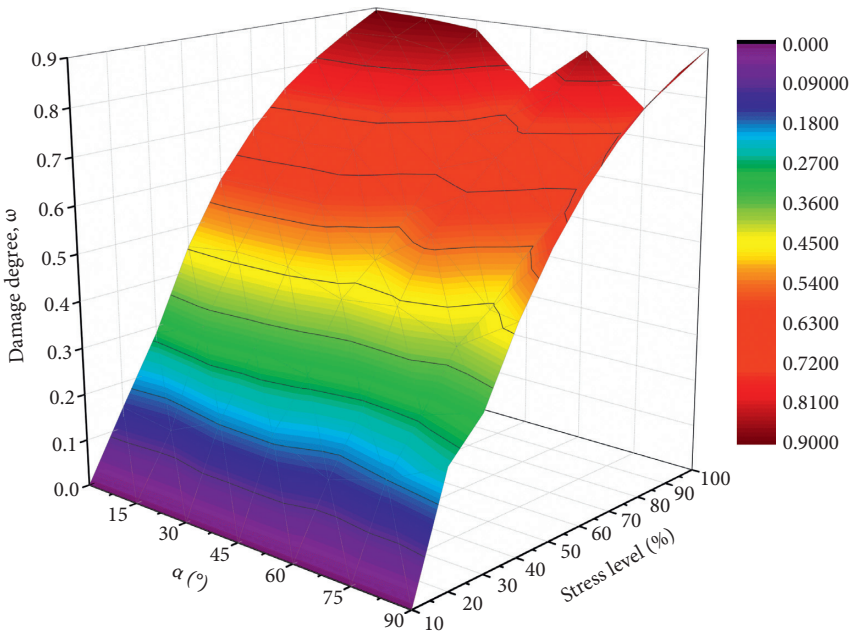

Figure 18: Relationship among damage degree, joint angle, along with stress level.

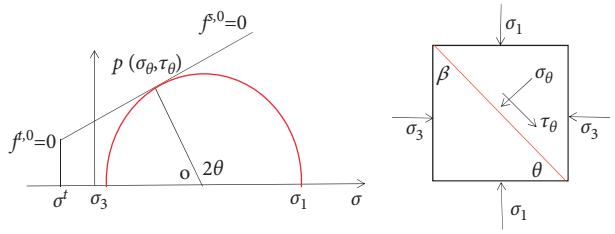

Figure 19: Theoretical analysis diagram of single joint sandstone.

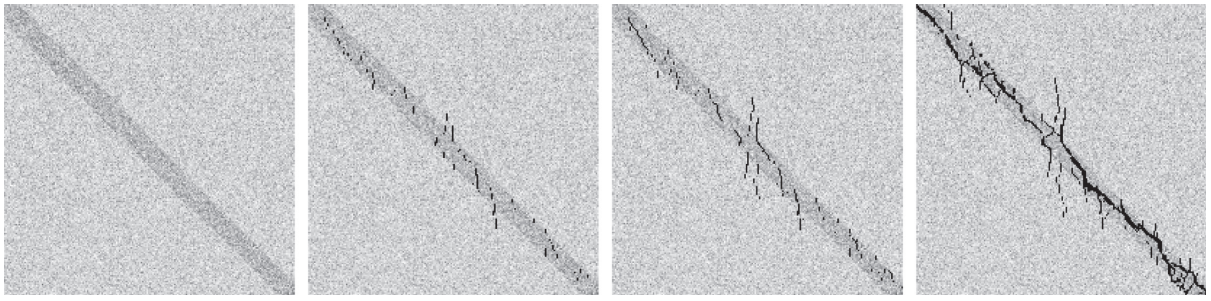

Initial model | Crack initiation | Crack propagation | Crack penetration

Figure 20: Fracture process of single joint sandstone.

procedure is fractal, whereas fractal dimension is an attribute quantity reflecting the degree of material damage, respectively. The use of fractal theory in geotechnical engineering allows individuals to have a better knowledge of the rock itself. The box dimension based on the acoustic emission field is used as a parameter for describing rock mesoscale fracture, which not only solves the problem of difficult quantification of discontinuous interfaces in the rock but also associates the microcracks evolution in the rock with the macroscopic mechanical behavior that overcomes the disadvantages. According to the research of this paper, the author developed a digital image box dimension calculation program, which can be utilized for calculating fractal dimension to analyze the mechanical characteristics of rock damage, in order to further reveal the rock's failure mechanism.

7. Conclusion

(1) On the basis of digital image storage and box size theory, MATLAB is used to develop a rock dimension algorithm based on a digital picture for the mesoscale failure box and establishes a mesoscale fracture damage assessment index based on an acoustic emissions field box dimension. This approach may be used for explaining the progression of rock mesoscale failure in quantitative terms, and the bigger the fractal dimension, the more the rock damage.

(2) The compressive strength and elastic modulus of jointed sandstone have obvious anisotropy, and they all change in U shape with the rise of joint dip angle. There are 6 final failure modes of samples: V-shaped ($\alpha = 75^{\circ}$), oblique Z-shaped ($\alpha = 0^{\circ}$), linear ($\alpha = 45^{\circ}$, $\alpha = 75^{\circ}$), oblique N-shaped ($\alpha = 90^{\circ}$), N-shaped ($\alpha = 60^{\circ}$), and M-shaped ($\alpha = 15^{\circ}$).

(3) In the present study, the oblique N-shaped failure mode has a fractal dimensional value of 1.80 and that is the greatest. The linear failure mode has 1.52 fractal dimension value, the smallest value. Between these two values are the fractal dimensions of M-shaped, N-shaped, V-shaped, and oblique *Z* modes. The fractal size may effectively define the failure mode of the joined sandstone, which demonstrates that the bigger the fractal size, the more complicated the rock failure mechanism.

(4) When the acoustic emission field is used as a parameter for characterizing rock mesoscale failure, the evolution of rock mesoscale failure is connected to macromechanical behavior evolution, which overcomes the problem of other damage definition techniques that require several rock characteristic parameters and provides a new way for quantitatively evaluating the damage degree of rock acoustic emission field

(5) AE energy increases with the increase of load and reaches the maximum near peak strength. This is because the greater the load is, the more the elements are damaged, the more the elastic energy is released, the denser the AE energy distribution is, and the more severe the internal damage is. When $\alpha = 90^{\circ}$, the AE energy distribution is the densest, is denser in the interval of $\alpha = 0^{\circ}$~45°, and finally is relatively sparse in the interval of $\alpha = 60^{\circ}$~75°. Accumulative AE energy increases exponentially with the increase of loading step, and the growth process can be divided into gentle period, acceleration period, and surge period.

Data Availability

Some or all data, models, or code generated or used during the study are available from the corresponding author upon request.

Conflicts of Interest

The authors declare that there are no conflicts of interest regarding the publication of this paper.

Acknowledgments

This study was supported by the program of China Scholarships Council (no. 202006670005), the Guizhou Province Science and Technology Support Program Project (no. QIANKEHE Support [2021] General 516), the National Natural Science Foundation of China (project nos. 51774101, 51574093, and 41962008), Scientific and Technological Innovation Talents Team in Guizhou Province (project no. [2019]5619), and the Guizhou Province High-Level Innovative Talents Training Project (Grant no. JZ2016-4011).

References

[1] Z. Wu, Y. Zuo, S. Wang et al., "Numerical simulation and fractal analysis of mesoscopic scale failure in shale using digital images," *Journal of Petroleum Science and Engineering*, vol. 145, pp. 592–599, 2016.

[2] T. -T. Wang and T. -H. Huang, "A constitutive model for the deformation of a rock mass containing sets of ubiquitous joints," *International Journal of Rock Mechanics and Mining Sciences*, vol. 46, no. 6, pp. 521–530, 2009.

[3] C.-C. Chiu, M.-C. Weng, and T.-H. Huang, "Modeling rock joint behavior using a rough-joint model," *International Journal of Rock Mechanics and Mining Sciences*, vol. 89, pp. 14–25, 2016.

[4] J. Meng, J. Huang, S. W. Sloan, and D. Sheng, "Discrete modelling jointed rock slopes using mathematical programming methods," *Computers and Geotechnics*, vol. 96, pp. 189–202, 2018.

[5] Y. Lou, Z. Wu, W. Sun et al., "Study on failure models and fractal characteristics of shale under seepage-stress coupling," *Energy Science & Engineering*, vol. 8, no. 5, pp. 1–16, 2020.

[6] H. Yang, J. Liu, and B. Liu, "Investigation on the cracking character of jointed rock mass beneath TBM disc cutter," *Rock Mechanics and Rock Engineering*, vol. 51, no. 4, pp. 1263–1277, 2018.

[7] G. Reik and M. Zacas, "Strength and deformation characteristics of jointed media in true triaxial compression," *International Journal of Rock Mechanics and Mining Science & Geomechanics Abstracts*, vol. 15, no. 6, pp. 295–303, 1978.

[8] X. S. Sun, J. L. Li, L. H. Wang, J. L. Bai, and Z. R. Jiang, "Experimental research on anisotropic mechanical characteristic of samples with single prefabricated joint," *Rock and Soil Mechanics*, vol. 35, no. Supp.1, pp. 29–34+41, 2014.

[9] Q. X. Kun, Li. C. Cong, and C. Zhang, "Study of the failure mode of a jointed rock mass due to a stress wave," *Advances in Civil Engineering*, vol. 2021, Article ID 1342691, 12 pages, 2021.

[10] P. L. P. Wasantha, P. G. Ranjith, D. R. Viete, and L. Luo, "Influence of the geometry of partially-spanning joints on the uniaxial compressive strength of rock," *International Journal of Rock Mechanics and Mining Sciences*, vol. 50, pp. 140–146, 2012.

[11] K. Morteza, R. Ahmad, and Z. Shokrollah, "Effects of joint orientation and spacing on the boreability of jointed rock

mass using tunnel boring machines," *Arabian Journal of Geosciences*, vol. 14, no. 1, pp. 1–14, 2021.

[12] F. As'habi and A. Lakirouhani, "Numerical modeling of jointed rock samples under unconfined and confined conditions to study peak strength and failure mode," *Arabian Journal of Geosciences*, vol. 14, no. 3, p. 1, 2021.

[13] Z. Z. Liang, C. N. Tang, and S. B. Tang, "Fractal and percolation evolution characteristics of rock damage process," *Chinese Journal of Geotechnical Engineering*, vol. 29, pp. 1386–1391, 2007.

[14] X. I. E. He-ping, *Fractal-rock Mechanics*, Science Press, Beijing, China, 1997, in Chinese.

[15] S. G. Zhang, X. D. Zhang, and F. Yi, "A timely damage and fractal evolution rule of uniaxial compression for frozen soil," *Rock and Soil Mechanics*, vol. 24, pp. 185–187, 2003.

[16] Y. Zhao, "Crack pattern evolution and a fractal damage constitutive model for rock," *International Journal of Rock Mechanics and Mining Sciences*, vol. 35, no. 3, pp. 349–366, 1998.

[17] S. J. Li, D. Li, L. Wu, and L. J. Cao, "Mesoscopic simulation and fractal characteristics of failure process in heterogeneous rock uniaxial compression test," *Journal of China Coal Society*, vol. 39, pp. 849–854, 2014.

[18] K. Zhang, X. H. Liu, K. Li, and W. Wu, "Relationship between mechanical properties of fractured multi-fracture rocks and fracture fractal dimension," *Chinese Journal of Rock Mechanics and Engineering*, vol. 37, pp. 2785–2794, 2018.

[19] A. H. Hofstra and J. S. Cline, "Characteristics and models for carlin-type gold deposits," *Gold in 2000*, vol. 13, pp. 163–220, 2000.

[20] J. S. Cline, A. H. Hofstra, J. L. Muntean, M. T. Richard, and A. H. Kenneth, "Carlin-type Au deposits in Nevada: critical geologic characteristicsand viable models," *Economic Geology 100th Anniversary*, vol. 1, pp. 451–484, 2005.

[21] J. L. Muntean, J. S. Cline, A. C. Simon, and A. A. Longo, "Magmatic-hydrothermal origin of Nevada's Carlin-type gold deposits," *Nature Geoscience*, vol. 4, no. 2, pp. 122–127, 2011.

[22] X. H. Luo, "The features of F3 ore-controlling fault and the mechanism of tectonic mineralization in Lannigou gold deposit, Zhenfeng County, Guizhou," *Geology of Guizhou*, vol. 10, no. 26–34, 1993, in Chinese with English abstract.

[23] Z. Li, L. Li, B. Huang et al., "Numerical investigation on the propagation behavior of hydraulic fractures in shale reservoir based on the DIP technique," *Journal of Petroleum Science and Engineering*, vol. 154, pp. 302–314, 2017.

[24] H. Liu, Y. J. Zuo, Z. H. Wu, and W. Sun, "Fractal analysis of mesoscale failure evolution and microstructure characterization for sandstone using DIP, SEM-EDS, and micro-CT," *International Journal of Geomechanics*, vol. 21, no. 9, Article ID 04021153, 2021.

[25] J. Lemaitre, "Evaluation of dissipation and damage in metals subjected to dynamic loading," in *Proceedings of the International Conference on Mechanical*, vol. 1, pp. 15–20, Kyoto, Japan, August 1971.

[26] C. A. Tang, L. G. Tham, S. H. Wang, H. Liu, and W. H. Li, "A numerical study of the influence of heterogeneity on the strength characterization of rock under uniaxial tension," *Mechanics of Materials*, vol. 39, no. 4, pp. 326–339, 2007.

[27] W. C. Zhu, J. Liu, C. A. Tang, X. D. Zhao, and B. H. Brady, "Simulation of progressive fracturing processes around underground excavations under biaxial compression," *Tunnelling and Underground Space Technology*, vol. 20, no. 3, pp. 231–247, 2005.

[28] X. H. Xu, S. P. Ma, M. F. Xia, F. J. Ke, and Y. L. Bai, "Synchronous multi-scale observations on rock damage and rupture," *Theoretical and Applied Fracture Mechanics*, vol. 44, no. 2, pp. 146–156, 2005.

[29] G. Li and C.-A. Tang, "A statistical meso-damage mechanical method for modeling trans-scale progressive failure process of rock," *International Journal of Rock Mechanics and Mining Sciences*, vol. 74, pp. 133–150, 2015.

[30] G. Li, C.-A. Tang, and Z.-Z. Liang, "Development of a parallel FE simulator for modeling the whole trans-scale failure process of rock from meso- to engineering-scale," *Computers & Geosciences*, vol. 98, pp. 73–86, 2017.

[31] C. Tang, "Numerical simulation of progressive rock failure and associated seismicity," *International Journal of Rock Mechanics and Mining Sciences*, vol. 34, no. 2, pp. 249–261, 1997.

[32] S. Y. Wang, S. W. Sloan, D. C. Sheng, and C. A. Tang, "Numerical analysis of the failure process around a circular opening in rock," *Computers and Geotechnics*, vol. 39, pp. 8–16, 2012.

[33] S. Y. Wang, S. W. Sloan, C. A. Tang, and W. C. Zhu, "Numerical simulation of the failure mechanism of circular tunnels in transversely isotropic rock masses," *Tunnelling and Underground Space Technology*, vol. 32, pp. 231–244, 2012.

[34] W. Weibull, "A statistical distribution function of wide applicability," *Journal of Applied Mechanics*, vol. 18, no. 3, pp. 293–297, 1951.

[35] F. Rossi, A. Di Carlo, and P. Lugli, "Microscopic theory of quantum-transport phenomena in mesoscopic systems: a Monte Carlo approach," *Physical Review Letters*, vol. 80, no. 15, pp. 3348–3351, 1998.

[36] R. Y. Rubinstein and D. P. Kroese, *Simulation and the Monte Carlo Method*, John Wiley & Sons, Hoboken, NJ, US, 2011.

[37] H. Diao, "Rock mechanical properties and brittleness evaluation of shale reservoir," *Acta Petrologica Sinica*, vol. 29, pp. 3300–3306, 2013.

[38] J. Wang, Y. Li, W. D. Song et al., "Analysis of damage evolution characteristics of rock masses with different dip angles," *Journal of Harbin Institute of Technology*, vol. 1-10, 2019.

[39] B. Liu and Y. Ning, "Application of fractal theory to geotechnical engineering," *Applied Mechanics and Materials*, vol. 52-54, pp. 1291–1295, 2011.

[40] H. Xie, *Fractals in Rock Mechanics*, A A Balkema, Rotterdam, 1993.

[41] J. Li, Q. Du, and C. Sun, "An improved box-counting method for image fractal dimension estimation," *Pattern Recognition*, vol. 42, no. 11, pp. 2460–2469, 2009.

[42] H. Xie, *An Introduction to Fractal - Rock Mechanics*, Science Press, Beijing, China, 1996.